MARES – Satellite-based microwave remote sensing for marine litter mapping

contract ESA STAR 2-1806/21/NL/GLC/ov

Executive summary

***Abstract*— Plastic marine litter is becoming a major environmental concern. Microwaves (MW) have potential for remote detection of floating macroplastics operating from Satellites or Airborne platforms, but very scarce and limited studies exist in the literature using MW. We present the first results of a systematic study on MW scattering of floating low-mass macroplastics at 2-20 GHz frequency band using radar techniques. Data was first collected in small-scale measurement campaigns carried out in an indoor facility capable of producing deep sea-like wave patterns, with different floating single-use plastic items. The study revealed that, for these targets, one important scattering contribution arises from the indentation they produce on the water. For the tested conditions, targets, and metrics, it was possible to detect several types of floating plastic targets down to 10 g/m^2 concentration. Detection tended to significantly improve at the X-band, although the detection threshold depends on the combination of the mentioned conditions. Tests were extended also to a small- and medium-scale outdoor scenarios with natural wind and capillary waves. Detection of macroplastics was successful in these tested scenarios. Also, passive radiometric tests were conducted at the W-band and showed very promising detection for floating plastics in small-scale outdoor environments. Finally, Machine Learning techniques were successfully evaluated as a complementary technique to improve the detection process, or the detection criteria.**

***Index Terms*— active radar, backscattering, macroplastics, marine plastics, polarimetry, microwave sensing, polarization, pollution, remote sensing, rough surface, scattering measurements, sea scattering, passive mm-wave sensing, Machine Learning.**

I. Introduction

Several million tons of mismanaged plastic waste enter the oceans every year [1], from rivers, untreated sewage discharge, and other watercourses. Over time, ocean currents pull plastic objects over long distances, allowing litter to drift around the oceans, eventually ending up in remote locations far away from its entry point, as for instance the Great Pacific Garbage Patch (GPGP) [2]. Such plastic accumulations, comprising a broad range of types and sizes, from meters to the nanoscale, may extend for thousands of square kilometers in area. Moreover, plastic waste is durable and contains toxic materials, entailing a wide range of problems, such as ecological, economic, social, or human health related.

Ocean cleaning and marine life preservation is one of the goals set by the United Nations in the 2030 Agenda for Sustainable Development under SDG 14 [3]. Detection of marine litter is presently being carried out from shore, ships, airplanes, unmanned aerial vehicles, sensing nodes, and a limited number of satellites [4]. Yet only satellites can provide the needed geographical reach. Despite the urgency, the topic of remote unsupervised detection of floating marine waste is still at its infancy. There is not yet enough evidence on the most appropriate technology for remote detection of marine litter; most probably, only combined information from multiple sensor technologies will be effective, given the variety and nature of marine debris.

Most of current research is focused on satellite-based optical sensing, in the visible and infrared spectrum [4]-[15]. However, these techniques are easily hampered by poor weather, light conditions, and bio fouling, preventing continuous scanning. Microwave sensing emerges as an alternative or complementary technique for detecting floating macroplastics – plastic items larger than 5 cm. Among its advantages, MW sensing does not suffer major atmospheric impairments, and relies on mature technology used for several land and sea Earth Observation missions [7], [8], [16], [17] and it also finds applications for marine target localization using radar techniques [18].

However, separating the plastic MW response from the ocean surface response is challenging. In fact, the sea surface has a high reflective response, given its high electric permittivity ($\varepsilon_r \approx 64$ @ $4\ GHz$) and conductivity ($\sigma \approx 9.8$ @ $4\ GHz$) [19]. Moreover, its surface is highly dynamic making scattering dependent on sea state, angle of incidence and frequency [20]. Therefore, it may overwhelm the plastic response, because of its relatively low concentration, despite the total amount in the oceans being colossal. In fact, studies report that macroplastics concentration in the GPGP in 2015-2016 was in the order of

This research was supported by ESA under contract ESA STAR 2-1806/21/NL/GLC/ov and Fundação para a Ciência e a Tecnologia-FCT/MCTES and co-funded by FEDER – PT2020 partnership agreement under project UIDB/50008/2020

.

700 items/km^2, corresponding to 0.015 g/m^2, and these quantities are exponentially increasing with time [2]. The concentration value reported in [2] was calculated as the average mass of the litter over the entire area travelled by the vessel. As a result, it does not represent the concentration at smaller areas where litter tends to form clusters. Additionally, plastic food ware, like water bottles, containers, etc. have both very low-mass and low electric permittivity ($\varepsilon_r \approx 2.1$ @ $4\ GHz$ [22], [23]), thus, these are expected to produce a weak MW response.

Only recently this topic gained interest of the research community [24]-[26], but the number of papers is scarce. The generality of the conclusions is limited, on the one hand because the analysis refers to a single or very few scenarios; on the other hand, the parameters of the spaceborne instrument, like the operation band, are previously fixed for other uses. This does not allow determining the best parameters, or the best methods of detection.

Therefore, our approach in this paper is to start from controlled small-scale measurements conditions, identify the scattering mechanisms and parameter dependence, establish an analytical formulation to separate the targets from the water response, and successively scale up to less controlled outdoor measurements. We also extend the study to passive radiometric sensing, as we believe that the most reliable detection comes from the combination of the results of different techniques. This is the novelty of our work, as there is no such basic information in literature.

Finally, we dedicate a part of the study to evaluate the potential of using Machine Learning to complement the traditional tools for target detection, given the difficult challenge to separate the response of very sparce targets from the strong response form the ocean surface,

II. Problem Formulation and Metrics

This section presents the generic geometry, problem formulation, involved parameters, and metrics for quantitative assessment of the results. The basic underlying principle is that a MW airborne or spaceborne instrument will never be able to detect individual targets of the type described in the previous Section due to its reduced cross-section and sparse distribution. Instead of imaging-based detection like SAR, we envisage a scattered energy-based metric, corresponding to the response of an ensemble of possibly sparse targets distributed within the antenna footprint. The detection will result from the comparison of this global scattered energy against the energy scattered by a reference background.

A. Problem formulation

Consider Figure 2 which presents the geometry of the studied scenario. The coordinate system is positioned at the average water level ($y = 0$). The water waves travel along the z-axis, with a surface height distribution following typical open-sea wave pattern, with a prescribed spectrum [28]. It is characterized by significant wave height H_s, and average period of T_s. The water surface is illuminated by N_a broadband antennas placed at height H_a above the average water level. The maximum of the antennas' radiation pattern is directed towards a common reference point $(x_0, y_0 = 0, z_0)$, thus, to a common illumination area on the water surface. The look angle is $\psi = \arctan(D/H_a)$, where D is the horizontal distance from each antenna to (x_0, y_0, z_0), and d is the slant distance. The β angle represents the azimuth observation angle relative to the propagation direction of the water waves.

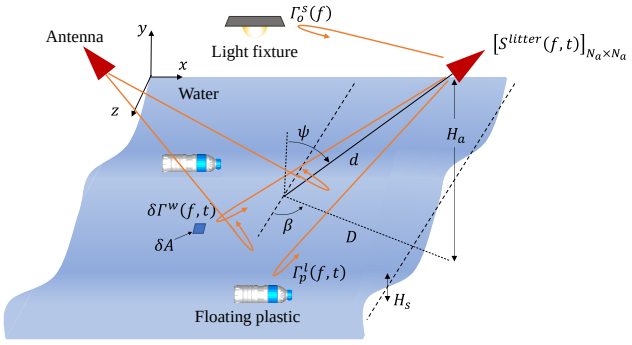

Figure 2: Main geometry of the problem, depicting the water surface, the antennas, and different scatterers.

The antennas are connected to a vector network analyzer (VNA) that retrieves the $N_a \times N_a$ complex scattering matrix, $\boldsymbol{S^{litter}}(f,t)$, for N_f frequencies swept in the $\Delta f = [f_{min}, f_{max}]$ band. The time sweep duration is δt, which is restarted N_t successive times. For simplicity we call each sweep a time sample t_u, and the S-matrix elements are referred to as S_{ij}. The S_{ij} signal emitted and captured by the i-th and j-th antennas, respectively, and received at time sample t_u comprises the contribution from all scatterers in the scenario, which includes the water dynamic surface, the floating litter, and other unwanted surrounding objects from the measurement scenario (i.e. walls, ceiling, floor, light fixtures, handrails, etc.). Assume that the water surface is composed of infinitesimal tilted "mirrors" of area δA characterized by a scattering coefficient $\delta\Gamma^w(f,t)$. Also, assume that there are N_o static objects in the scenario and N_p floating plastic objects. The o-th static scatterer and p-th plastic object are characterized by their scattering coefficients $\Gamma_o^s(f)$ and $\Gamma_p^l(f,t)$, respectively, each dependent on its shape and orientation. Assuming very low litter concentration (which is the case of interest to establish a minimum detection threshold), the measured $S_{ij}^{litter}(f,t)$ may be expressed at time sample t_u as

$$S_{ij}^{litter}(f,t_u) = \Gamma^w(f,t_u) + \sum_{o=1}^{N_o} a_o \Gamma_o^s(f) + \sum_{p=1}^{N_p} a_p \Gamma_p^l(f,t_u) \quad (1)$$

where $\Gamma^w(f,t_u)$ is the total contribution from all M "water mirrors" contained in the antenna footprint bearing favorable tilt towards the receiving antenna:

$$\Gamma^w(f,t_u) = \sum_{m=1}^{M} a_m \delta\Gamma_m(f,t_u) \quad (2)$$

The reflection coefficients of the scatterers depend on the ij-th antenna pair. Moreover, a_o, a_m and a_p coefficients involve

the distance to the antenna, and the antennas' radiation patterns. The contribution from the water and floating plastics is a function of time due to the water dynamics. The contribution from unwanted clutter in the measurement scenario is considered static and may be significantly higher than the energy scattered by the water and plastic objects, i.e. $|\Gamma_o^s| > |\Gamma^w|$ and $|\Gamma_o^s| \gg |\Gamma_p^l|$. It is essential to remove those contributions from the *S*-matrix, to retrieve only the scattering information from water and plastics. To this end, in each of the addressed cases, we measured the *S*-matrix immediately before introducing the plastic litter. These measurements, considered as reference measurements, and those containing the plastic influence, are labelled $\boldsymbol{S}^{\boldsymbol{ref}}(f,t)$ and $\boldsymbol{S}^{\boldsymbol{litter}}(f,t)$, respectively. To remove the effect of the static components from the S_{ij}, both matrices are calibrated as follows:

$$\boldsymbol{S}^{\boldsymbol{cal,ref}}(f,t_u) = \boldsymbol{S}^{\boldsymbol{ref}}(f,t_u) - \langle \boldsymbol{S}^{\boldsymbol{ref}}(f,t_u) \rangle \quad (3.a)$$

$$\boldsymbol{S}^{\boldsymbol{cal,litter}}(f,t_u) = \boldsymbol{S}^{\boldsymbol{litter}}(f,t_u) - \langle \boldsymbol{S}^{\boldsymbol{ref}}(f,t_u) \rangle \quad (3.b)$$

where t_u represents one time sample and $\langle \cdot \rangle$ represents a time-average over all N_t time samples from the reference.

B. Evaluation metrics

We need to define metrics to enable comparing and ranking the different cases under analysis and identifying those corresponding to positive detection of plastic litter. We introduce two metrics, one based on the scattered signal energy, and another based on statistical analysis of the retrieved amplitudes. Both are related, although providing different insight into the results.

1) Energy-based metric

We define the following intensity function for each time sample t_u and for each distance pair d_i and d_j from the *i*-th and *j*-th antenna to a scattering point in the water surface:

$$I_{ij}(d,t_u) = \left| \frac{1}{n_f} \sum_{q=1}^{n_f} S_{ij}(f_q,t_u) e^{jk_{0,q}2d} \right|^2 \quad (4)$$

where n_f is the number of measured frequencies in a given frequency sub-set, $\Delta f = [f_1, f_2]$, and $k_{0,q} = \frac{2\pi f_q}{c}$ is the free-space wavenumber at frequency f_q ($c = 3 \times 10^8\ m/s$ is the speed of light in vacuum), and $2d = d_i + d_j$ is a discretized averaged distance between the antennas and a migrating point over the water surface. This metric is calculated over a wide bandwidth, from 2 to 20 GHz, and at 2- and 3-GHz sub-bands to also highlight the dependence of the scattering response versus frequency. As it will become apparent ahead, there is no advantage in testing outside the 2 to 20 GHz range. For convenience, we use a non-standard frequency band naming for the 2-GHz sub-bands, listed in Table I.

Equation (4) is used both with $S_{ij}^{cal,ref}$ and $S_{ij}^{cal,litter}$, leading to $I_{ij}^{cal,ref}$ and $I_{ij}^{cal,litter}$, respectively. This is used to compute the following function that gives a measure of the energy scattered in a single sweep by the water plus targets at time sample t_u:

$$SEn_{ij}^{litter}(t_u) = \frac{1}{N_d} \sum_{d=d_{min}}^{d_{max}} I_{ij}^{cal,litter}(d,t_u) \quad (5)$$

where d_{max} and d_{min} correspond to the maximum and minimum distances from the antenna to the edges of the antenna footprint on the water and N_d is the number of discretized distance points used in the calculation.

Table I
FREQUENCY BANDS UNDER STUDY.

Frequency band designation	f_1 [GHz]	f_2 [GHz]
S-band	2	4
"C-under" band (Cu)	4	6
"C-above" band (Ca)	6	8
"X-under" band (Xu)	8	10
"X-above" band (Xa)	10	12
"Ku-under" band (Kuu)	12	15
"Ku-above" band (Kua)	15	18
K band (K)	18	20
Ultrawideband (UWB)	3.1	10.6

Summing over successive time samples, gives a measure of the total energy scattered by the water plus targets in the antennas' footprint over a certain time integration interval:

$$En_{ij}^{litter} = \frac{1}{N_t} \sum_{u=1}^{N_t} SEn_{ij}^{litter}(t_u) \quad (6)$$

This is used both with $I_{ij}^{cal,ref}$ and $I_{ij}^{cal,litter}$, leading to En_{ij}^{ref} and En_{ij}^{litter}, respectively. Lastly, we calculate an energy ratio (EnR) based on the *ij*-th scattering parameter as

$$EnR_{ij} = \frac{En_{ij}^{litter}}{En_{ij}^{ref}}. \quad (7)$$

This figure of merit allows comparing the scattering of water with and without floating litter, under the same conditions. The presence of litter is expected to add to the water surface roughness, thus, increasing EnR_{ij}. This increase was confirmed experimentally. Therefore, whenever $EnR_{ij} > EnR_{threshold}$, where $EnR_{threshold}$ is a threshold to be established, it is interpreted as positive detection of floating litter. The case $1 < EnR_{ij} < EnR_{threshold}$ means the opposite. The case $EnR_{ij} < 1$ would correspond to wave dampening, but this was not found in the tested cases. It remains to define the EnR threshold, $EnR_{threshold}$, at which we can consider that the litter is detected. This will be detailed ahead, when discussing the results.

2) Statistical metric

We use the nonparametric Kolmogorov-Smirnov test (KS), which allows to determine the probability that two sets of measured samples follow the same unknown probability distribution [29]. This test is used to compare the distribution functions associated with reference $I_{ij}^{cal,ref}$ and litter $I_{ij}^{cal,litter}$. High values of the maximum absolute difference between the two cumulative distribution functions should be indicative of litter presence. The KS test is an alternative metric used to confirm the energy-based conclusions drawn with the EnR. As with the *EnR* metric, the detection threshold $KS_{threshold}$ based on the KS test will be addressed ahead, when discussing the measured results.

III. PLASTIC SCATTERING IN FLAT WATER CONDITIONS

This section discusses the initial measurements carried out in a small controlled outdoor scenario with static fresh water. This allowed to identify the main scattering mechanisms of floating plastic litter, without the perturbation from dynamic water contributions. The interest is on objects with low mass-to-surface ratio, to establish minimum detection thresholds. The used targets are typically extremely low mass plastic waste, like table bottles, straws, insulating foams, or fast-food containers. The tests cover the dependence with the target shape, orientation, and size.

A. Setup and targets description

Measurements in static water conditions were carried out in the setup represented in Figure 3 (a), at Instituto de Telecomunicações in Lisbon, Portugal. It is a 4.5 × 2.1 × 0.8 m^3 garden pool, with water height limited to 0.2 m to 0.23 m. The MW illumination was obtained with a single dual-polarized (vertical and horizontal electric field components) ridged horn that is impedance-matched over the 2-20 GHz frequency band (QRH20E [30]). The antenna gain ranges from approximately 6.5 dBi, at 2.5 GHz, up to about 14.5 dBi, at 15 GHz, in both polarizations. The cross-polarization and port isolation are better than -30 dB and -35 dB, respectively, across the entire bandwidth. The antenna was mounted at the shortest side of the pool, at $H_a = 2.1\ m$ height from the water surface, with a look angle of $\psi = 37°$. This height is the maximum we can extend the antenna's tripod, and the angle ensures that the antenna footprint points at the middle of the pool, thus minimizing the contribution from the highly scattering corners of the pool. The two ports of the antenna were connected to an Agilent e5071c VNA that acquired the 2 × 2 scattering matrix for VV, VH and HH data. We measured an average of $N_t = 104$ measurement sweeps per testcase, with an average time step $\delta t \approx 3.48\ s$. The frequency sweep ranged from 1.5 GHz to 14 GHz, with $N_f = 1601$ frequency points.

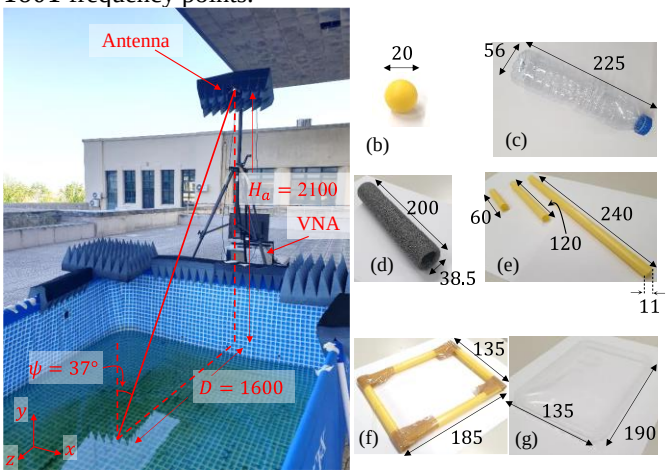

(a)

Figure 3: (a) Photograph of the measurement setup used for static water conditions; (b) PP plastic sphere; (c) PET plastic bottle; (d) PE cylinder foam; (e) plastic straws; (f) plastic straw frame; (g) plastic lid. Dimensions are in millimeters.

In the tests, the water surface was approximately flat ($H_s \approx 0$) and the targets were floating at a constant horizontal distance $D \approx 1.6\ m$ from the antenna. We tested several types of floating plastics, but we present here only six of them (see Figure 3), which are relevant to highlight some features of the scattering mechanism: (b) 10 mm radius polypropylene sphere (PP, $\varepsilon_r \approx 2.26$ @ 10 GHz [24]); (c) 500 ml polyethylene terephthalate bottle (PET, $\varepsilon_r \approx 3.1$ @ 15 GHz [24]), 225 mm high, and 28 mm radius; (d) polyethylene cylindrical foam tube (PE, $\varepsilon_r \approx 1.5$ @ 10 GHz [24]) with outer and inner diameters of 38.5 mm and 23 mm, respectively, and length of 200 mm; (e) plastic straws with length $L = 240, 120, 60\ mm$ and radius of 5.5 mm; (f) rectangular frame made of plastic straws with dimensions of 185 × 135 mm; (g) lastly, 190 × 135 mm PET lid from a fast food box.

B. Scattering components

First tests showed that small objects such as floating expanded polyethylene (PE) foam have a detectable radar signature, as seen ahead, for instance in Fig. 6. We will explain next how such a low-contrast, low-mass material can have significant MW signature. We start with the backscatter of the most basic target, a single floating plastic sphere, which is used as a reference for subsequent measurements. In the following figures, we represent $I_{ij}^{cal,litter}(d, t_u)$ at a single time instant t_u; hence, we omit the dependency on time and designate it as $I_{ij}^{cal,litter}(d)$ for simplicity. Figure 4 shows an example of acquired $I_{ij}^{cal,litter}(d)$, in VV polarization, versus the radial distance measured from the antenna phase center. The sphere response is clear at about 2.47 m. Although $I_{ij}(d, t_u)$ is dimensionless, it is proportional to the energy scattered by the sphere, therefore the maximum in Figure 4 is a useful reference for comparison with other targets. The non-zero response away from the sphere position is due to shallow ripple on the water caused by air breeze.

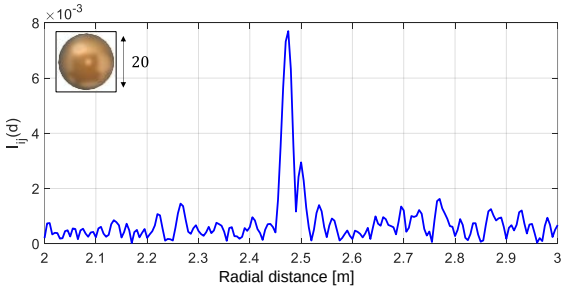

Figure 4: Measured magnitude of VV scattering energy, $I_{ij}^{cal,litter}(d, t_u)$, by a single PP sphere floating on water. The abscissa is the slant distance from the antenna to the sphere. The inset shows the sphere dimensions in millimeters.

We present in Figure 5 the VV intensity $I_{ij}^{cal,litter}(d, t_u)$ of a table plastic bottle, when floating, and when suspended 1 cm above water using a thin 0.25 mm nylon thread, exactly at the same position and orientation. The intensity is normalized to the maximum of the plastic sphere response in Figure 4 (b). When suspended, the bottle's maximum intensity is like that of the sphere but increases 11 times when laid floating. This result has been confirmed through full-wave simulation, in which we modelled the experimental setup (not shown). This huge increase of the target response when laid floating, was observed consistently for the other tested plastic targets, despite the very low plastic material content ($< 10\ g$).

As a result of all tests, we identify two contributions for the scattering of floating macroplastics, in flat water: (i) the dielectric contrast at the air/plastic target interface, its effect being modulated by the surface shape, area, and incidence angle; (ii) the concave and meniscus indentations that the objects form on the water surface. The latter may have the major role in the total scattered field.

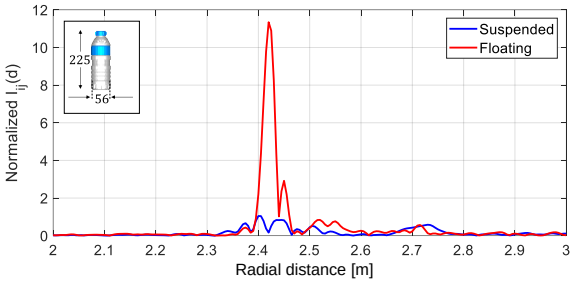

Figure 5: Normalized magnitude of VV scattered energy, $I_{ij}^{cal,litter}(d,t_u)$, by a single plastic bottle suspended 1 cm above water (blue) and floating on water (red). The inset shows the target's dimensions in millimeters.

C. *Dependence on shape and orientation*

The scattering cross section of an object naturally depends on its shape and orientation. As an example, we used the very thin plastic lid of a fast-food container. It comprises a 190×135 mm flat surface, and a rounded edge. Additionally, we have cut a similar lid, separating the flat part from the rounded edge; onwards we label them as lid, lid center and lid frame. Measuring their separate response provides more insight into the scattering mechanism. The results in Figure 7, for VV polarization, show that the lid and the lid frame exhibit maximum magnitudes of around 4 and 2 times to that of the reference sphere, respectively. For both objects, there are two peaks that we identify with the water indentation created by the lid frame. The backscatter from the thin lid center is 1.5 times higher response than the sphere, despite being flat in flat water. This originated by the water meniscus at the lid center edges. Tests carried out for different incidence angles showed changes in amplitude and distance between these peeks.

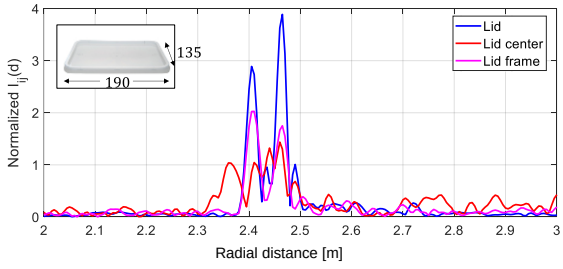

Figure 7: Normalized measured magnitude of VV scattered energy, $I_{ij}(d,t_u)$, by a plastic lid floating on water: complete lid (blue), lid center cut-out (red) and lid frame cut-out (mangenta). The inset shows the target's dimensions in millimeters.

D. *Dependence on the electrical size*

It is well-known that the radar cross section of a target is related to its electrical dimensions, which may increase with its electrical size in terms of wavelength. To assess the frequency dependence, we split the analysis into 2-GHz sub-bands defined in Table I. We measured the scattering intensity of a single plastic straw section of length $L = 200, 100, 50\,mm$ each, respectively. We also did the same for 1, 2 and 4 sections of polyethylene foam tubes of $L = 200, 100, 50\,mm$ each, respectively, distributed along the range axis. In this case, in each measurement, the total volume and mass of the floating objects remained approximately the same. In all cases, the objects' longest dimension was aligned with the antenna's cross-range direction.

Figure 9 compares the obtained normalized $I_{ij}^{cal,litter}(d,t_u)$ values, for each frequency sub-band. The response of straws is lower than the foam tubes, which is expected due to shallower water indentation of the straws. The response increases with the size of the individual target and generally increases with frequency. PE foam tubes additionally exhibit a resonance behavior which is related to the dimensions of the water indentation along the incidence plane.

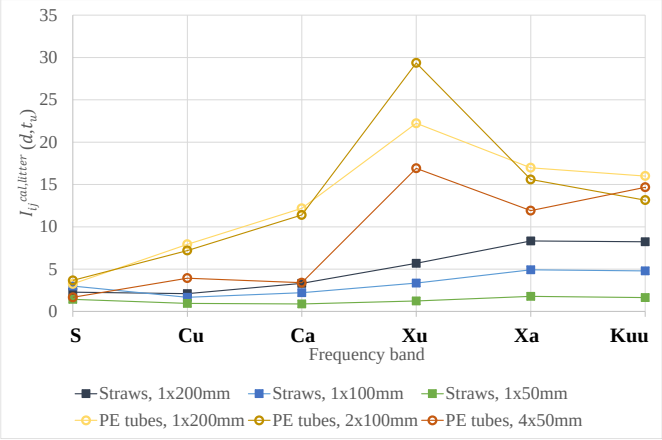

Figure 9: Maximum of the normalized magnitude of VV scattered energy, $I_{ij}^{cal,litter}(d,t_u)$ by plastic straws and polyethylene foam tubes with different lengths, keeping the same total mass between all tests. The normalized $I_{ij}^{cal,litter}$ is calculated for the indicated 2-GHz and 3-GHz sub-bands, and the value is represented by the marker. The lines between markers have no physical meaning; they just highlight the response trend *vs.* frequency.

E. *Discussion*

The interpretation of the results from this whole Section III indicates that for sparse floating objects with low dielectric contrast to air, the scattered signal is dominated by the water surface deformation they cause, the shape and the orientation of the indentations, and less by the plastic material itself. This points to an almost indirect detection of plastic for low concentrations, although the conclusions may be different for larger, carpet type, plastic concentrations, which may occur in dams or near-shore, but are not likely in deep sea. Another important observation is that the response appears to enhance for a preferential frequency band. This is relevant for the discussion of the dynamic water results ahead. Finally, we stress that in static water, detection of a single object is possible, being its size only limited by the receiver sensitivity.

IV. PLASTIC SCATTERING IN DYNAMIC WATER

Further to the previously identified scattering contributions from floating objects, dynamic water conditions add a strong contribution from its surface. In this section we apply the formulation and metrics of Section II to separate it from the plastic response. We work with the experimental response of a few of the previous targets, floating in a deep ocean-like wave scenario, in the absence of high frequency Bragg effects.

A. Setup description

These measurement campaigns were conducted at the Atlantic Basin of DELTARES facilities, in the Netherlands [27]. It is a $75\,m \times 8.7\,m$ flume, with $D = 1\,m$ deep fresh water, located inside a closed pavilion, therefore wind-free (Figure 10). The waves are generated by twenty computer-controlled wave paddles, located at one edge of the flume. They can generate any water wave spectrum with maximum significant heigh of $0.25\,m$, or regular waves with maximum wave height of $0.45\,m$, propagating along the flume length (our z-axis). A wave energy absorption system exists at the end of the flume to dampen water wave reflection.

(a)

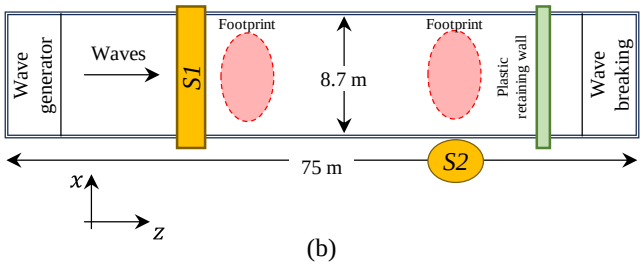

(b)

Figure 10: (a) General view of the Atlantic Basin in DELTARES facility. Photo [27], with permission; (b) Schematic of the setups' location over the basin.

We used two separate setups, which we label as *S1* and *S2* in Figure 10, corresponding to different locations of the antennas and equipment near the basin, with different β and ψ angles, frequency scanning intervals, number of frequency points, sweep times etc. In this summary, we concentrate just on the S1, with $\beta = 0°$, $\psi = 50°$, Freq. 2.5.20 GHz.

Setup1 was mounted near the mid-length of a bridge across the flume width, with $N_a = 3$ antennas positioned side-by-side at $H_a = 2.5\,m$ above the mean water level, with horizontal distance between each other $d_a = 1\,m$ (recall the geometry in Figure 2). The water waves were propagating along the antennas' range direction. The antennas were an ultrawide band, dual-polarization QRH20E antenna (ports 2 and 3), used in the flat-water tests, plus two V-polarized DRH30 antennas [30], [31] (ports 1 and 4) mounted with $1\,m$ horizontal separation from the central horn QRH20E. The gain of the V-pol antennas ranges from 6 dBi to 14 dBi across the band [2.5, 20] GHz. The antennas produced an elliptical footprint on the water surface, with -10 dB size in the order of 3 m and 4.5 m

Different mechanically generated water wave patterns were tested in the flume, but this study concentrates on the JONSWAP spectrum cases [28]. This spectrum describes a sea state resulting from the interaction of the ocean surface with sustained winds for a long period of time and over a large area. The parameters were selected to approximately verify the deep-sea condition: the peak of the spectral density function occurred at 0.8 Hz (corresponding to a period $T_s = 1.2\,s$ and wavenumber $k = 2.8$ rad/m). Therefore, $k\,D = 2.8$ rad, confirming the deep-sea claim. The high frequency cut-off was near 3 Hz. High-frequency Bragg-resonant effects were not included, because of technical limitations to produce artificial capillary waves indoor. However, Bragg effects are analyzed in Section VI in outdoor scenarios.

Tests were conducted for three significant heights, $H_s = 5, 9$ and $17\,cm$. Careful measurements showed that the spectral conditions were maintained from the wave generation plane up to the test region and were repeatable over time. For each test condition, measurements always started without any objects in the water, and continued while and after plastic litter was added behind setup *Setup1*. Measurements in the absence of plastic constitute the reference defined in Section II. On average, we logged $N_t^{ref} = 500$ times samples for each test, measured at 1-second time intervals. Targets were deployed immediately following the reference measurement, to minimize the impact of VNA drifts due to uncontrolled ambient temperature. We logged on average $N_t^{litter} = 1000$ time samples with litter. This measured data was calibrated using (3.a) and (3.b). In the satellite scenario, this sequence would correspond first to the continuous readings of the instrument in the absence of floating litter, and then the distinctive response after the antenna footprint entering a large patch of litter (response anomaly).

B. Detection threshold

One of the goals in the following sub-sections is to assess the detectability of floating plastics of different shapes/sizes, concentrations, wave heights, polarization, and frequency band. This requires a prior definition of a detection threshold in terms of both metrics introduced in Section II, $EnR_{threshold}$ and $KS_{threshold}$, below which we are not able to confidently distinguish the presence of litter.

We base this threshold on the uncertainty of the reference measurement over time, originated by uncontrollable variation of the environment and the setup itself. As an example, Figure 11 and Figure 12 show $I_{ij}^{cal,litter}(d, t_u)$ for $H_s = 5{,}9{,}17\,cm$ in the absence of targets (reference measurements), for setup *Setup1* and *Setup2* at 2-20 GHz and UWB frequency bands, respectively. We compute EnR and KS for all reference measurements, $\boldsymbol{S}^{\boldsymbol{cal,ref}}(f, t_u)$, taken on different days, or different times of the day, but with similar water conditions. The detection threshold for each H_s is set as the maximum value

of EnR and KS, among all measured references. Table II shows the obtained threshold values, for the studied frequency sub-bands, for both setups, and polarizations. The thresholds depend on wave height and detection frequency. Both metrics tend to increase the threshold with H_s. It also tends to increase with frequency towards the Xa to Kua bands and decrease beyond. These values are used in next subsections to analyze the effect of different parameters on plastic litter detectability.

These thresholds must be considered with caution, as they are derived for a controlled environment, with limited range of water surface roughness parameters and without wind. They depend on scenario conditions, and, therefore, they would have to be reassessed for other more complex scenarios, for instance with the presence of high-wavenumber wind effects.

It is worth noting that plastic concentration in the ocean is usually referenced in kg/km^2 [2]. However, it is not simple to translate our previously defined metrics to kg/km^2. In fact, given the analysis and conclusions so far, plastic mass does not seem to play a significant role on MW scattering of floating litter, at least for the very low concentrations that matter in open sea. For reference, we indicate in all tests the approximate concentration in g/m^2, and the number of used targets.

For clarity, in the next sections we try to separate the analysis by the factors that influence detectability, although they are all connected. We start by considering the full frequency band and, at the end, we break the analysis into sub-bands to select the most favorable ones.

C. *Effect of targets' shape and size*

We analyzed the detection of PP spheres, PE foam tubes (5 cm length), and PET bottles, using the full frequency band from [2, 20] GHz. We aimed at concentrations of 10 g/m^2 for the three types of targets, although it is not always easy to achieve due to the water dynamics, currents, etc. It corresponds approximately to 3 spheres/m^2, to 5 foam tubes of 5 cm in length/m^2, and to 1.3 bottles/m^2.

Table II
$EnR_{threshold}$ AND $KS_{threshold}$ FOR BOTH SETUPS, AT EACH FREQUENCY BAND UNDER STUDY AND FOR H_s = 5,9,17 CM.

Setup	Pol.	Freq. band	$ENR_{threshold}$			$KS_{threshold}$[%]		
			H_s [cm]			H_s [cm]		
			5	9	17	5	9	17
Setup1	VV	S	1.18	1.24	1.24	4.2	7.5	3.9
		Cu	1.20	1.25	1.22	6.6	7.4	7.2
		Ca	1.15	1.29	1.37	4.8	8.2	11.6
		Xu	1.10	1.36	1.51	3.9	9.2	12.9
		Xa	1.17	1.46	1.52	4.3	13.2	14.9
		Kuu	1.13	1.31	1.51	4.8	10.7	12.5
		Kua	1.39	1.27	1.35	7.7	10	7.4
		K	1.33	1.26	1.28	7.3	6	6.4
		2 - 20	1.11	1.31	1.36	3.4	9.2	9.1
	VH		1.06	1.13	1.13	2.3	4.1	4.4
	HH		1.11	1.14	1.21	3.5	4.5	6.3
Setup2	VV	Cu	1	1.07	1.17	1	2	9
		Ca	1.05	1.07	1.22	2	3	8
		Xu	1	1.11	1.21	1	3	11
		UWB	1.03	1.04	1.17	1	2	9

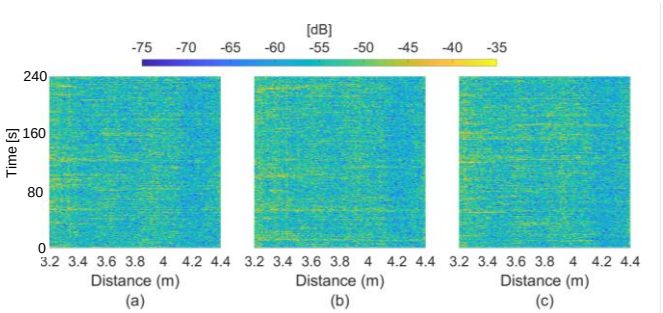

Figure 11: Scattered VV results, $I_{ij}^{cal,litter}$ in dB, based on $S_{1,4}(f)$ response measured in *Setup1* for reference case (i.e. no litter) using the entire 2-20 GHz frequency range: (a) $H_s = 5\ cm$; (b) $H_s = 9\ cm$; (c) $H_s = 17\ cm$.

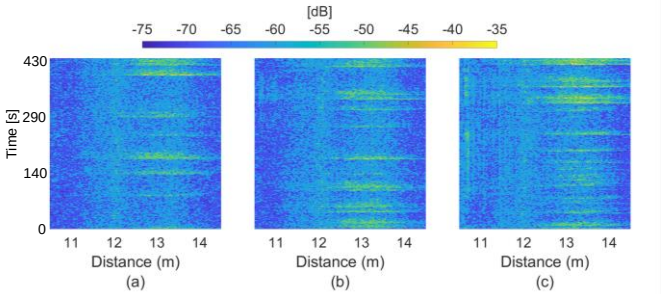

Figure 12: Scattered VV results, $I_{ij}^{cal,litter}$, using *Setup2* for reference case (i.e. no litter) and UWB in dB: (a) $H_s = 5\ cm$; (b) $H_s = 9\ cm$; (c) $H_s = 17\ cm$.

A custom-built ball dropping device was available at DELTARES to produce steady plastic spheres concentration over time. For all other types of plastic, concentrations were controlled manually. Figure 13 presents $I_{ij}^{cal,litter}$ results of *Setup1* for PE foam tubes, PET bottles, and PP spheres, in VV polarization. The abscissa represents the slant distance from the antennas to the water surface, while the ordinate corresponds to the successive time samples. The higher intensity (yellow) trails correspond to scattering from floating objects travelling away from the antenna (or, rather, the water indentation they form, as discussed earlier). These traces appear because the targets have persistent shape and slow velocity, while the water surface changes rapidly during each VNA frequency sweep, thus becoming averaged. The trails' slope gives a measure of each object's travel velocity. Given that the time sample interval is 1 *s*, the slopes indicate drift velocities between 0.02 m/s and 0.05 m/s. The theoretical Stokes's drift for these water conditions computes to 0.03 m/s, which confirms the claim.

Comparison of Figure 13 with Figure 11 makes it clear that it is the addition of floating targets that is responsible for the increased scatter and not the water dynamics. This visual information is reassuring that we are detecting actual items, and not image artifacts. Having said that, we stress, however, that plastic detection using our formulation requires only signal processing and does not rely on image processing.

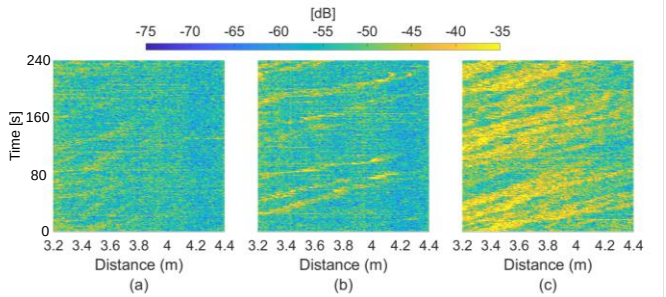

Figure 13: Scattered VV results, $I_{ij}^{cal,litter}$ in dB, based on $S_{1,4}(f)$ response measured in *Setup1*, with $H_s = 9\ cm$ at a concentration of 10g/m^2 and frequency band [2, 20] GHz in dB: (a) plastic spheres; (b) plastic bottles; (c) 5 cm length foam tubes.

EnR and KS metrics for this scenario are presented in Table IV. For all three types of targets, the values are above the threshold (Table III), therefore the detection is positive under this criterion. PE tubes present the largest scattering response, followed by PET bottles and lastly by PP spheres. This is explained in part by the larger number of foam tubes within the antenna's footprint compared to the bottles (for the same g/m^2 concentration), and partly by the objects' different scattering cross-sections as seen is the static water analysis, which penalizes spheres. This difference is also visually recognizable in Figure 13. It is interesting to note that we can visually detect individual PET bottles in Figure 13 (b), which is a good qualitative detection indicator by itself. It is also important to note that both metrics show similar trends with the different changes of the conditions or parameters. This observation holds for all cases we analyzed.

Table III
SCATTERING VV ENR AND KS RESULTS BASED ON $S_{1,4}(f)$ RESPONSE MEASURED USING *SETUP1* FOR $H_s = 9$ CM AT A CONCENTRATION OF 10G/M^2 AND FREQUENCY BAND OF [2, 20] GHZ.

H_s [cm]	Object [10 g/m^2]	Pol.	Freq. [GHz]	EnR	KS [%]
9	PP spheres	VV	2 - 20	1.45	9.6
	PET bottles			1.73	9.3
	5 cm PE tubes			9.93	39.3

Table IV
BACKSCATTERING VV ENR AND KS RESULTS USING *SETUP2* FOR $H_s = 9\ cm$ AT A CONCENTRATION OF 10 G/M^2 AND UWB FREQUENCY.

H_s [cm]	Object [10 g/m^2]	Pol.	Freq. [GHz]	EnR	KS [%]
9	PP spheres	VV	UWB	1.25	9
	PET bottles			2.81	13
	5 cm PE tubes			3.27	23

D. Dependence on polarization

For the polarization dependence study, we analyse the scattering from 5 cm PE foam tubes, and 12 cm plastic straws measured with the central dual-polarization horn. Figure 15 and Figure 16 present the $I_{ij}^{cal,litter}$ results obtained using VV, VH, and HH polarizations results for VV, VH, and HH polarizations, for cylinders and straws, respectively.

The cylinders and straws trails are visible for the three polarization states. The corresponding metrics are summarized in Table VI. EnR and KS numerical results indicate that, at least under the test conditions, VV polarization has a larger response than VH and HH, for both target types. For all polarizations states, PE tubes present higher response than straws. All values are above the threshold, indicating clear detection based on quantitative metrics.

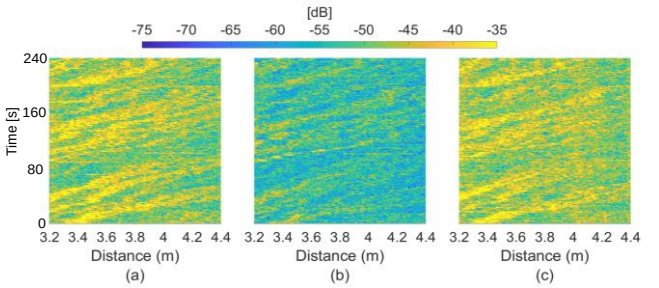

Figure 15: Foam tubes scattering results, $I_{ij}^{cal,litter}$, based on $S_{1,4}(f)$ response measured using *Setup1* for $H_s = 9\ cm$ at a concentration of 10 g/m^2 and frequency band [2, 20] GHz in dB: (a) VV; (b) VH; (c) HH.

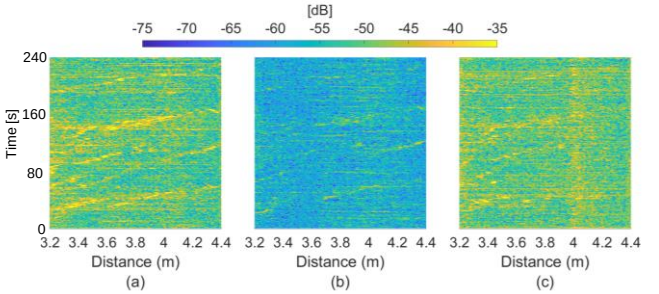

Figure 16: Plastic straws scattering results, $I_{ij}^{cal,litter}$, based on $S_{1,4}(f)$ response measured using *Setup1* for $H_s = 9\ cm$ at a concentration of 10 g/m^2 and frequency band [2, 20] GHz in dB: (a) VV; (b) VH; (c) HH.

Table V
SCATTERING VV, VH AND HH ENR AND KS RESULTS BASED ON $S_{3,3}(f), S_{2,3}(f)$ AND $S_{2,2}(f)$ RESPONSES, RESPECTIVELY, MEASURED USING *SETUP1* FOR DIFFERENT TARGETS FOR DIFFERENT POLARIZATIONS.

H_s [cm]	Object [10 g/m^2]	Pol.	Freq. [GHz]	EnR	KS [%]
9	5 cm PE tubes	VV	2 - 20	7.79	31.7
		VH		4.20	29.9
		HH		5.87	29.2
	12 cm straws	VV		2.14	12.7
		VH		1.27	5.8
		HH		1.65	9.7

E. Dependence on concentration and wave height

Thus far, the observations and conclusions refer to $H_s = 9\ cm$ with concentrations of 10 g/m^2. It remains to study the detectability with other concentrations in g/m^2. It should depend on H_s, given the increased surface roughness for larger H_s values. The higher the scattering from the water, the harder it becomes to separate the plastic contribution, therefore impacting negatively on the minimum detectable concentration.

The targets were PP spheres, since their concentration was accurately controlled using the sphere dropping device, and their scattering is independent of the observation angle, allowing to separate effects. We present results for 10 g/m^2, 20 g/m^2 and 40 g/m^2, although other intermediate values were also tested, but with lower control of the concentration. For conciseness, we omit the graphical representation of $I_{ij}^{cal,litter}$, and focus only on the metrics, as it would happen in remote automated measurement scenarios. Table VII summarizes the corresponding metrics results. The spheres are always detected for $H_s = 5\ cm$ and $H_s = 9\ cm$, suggesting that they might be detected for even lower concentrations (this was not tested). As for $H_s = 17\ cm$, the minimum detectable concentration is between 10 g/m^2 and 20 g/m^2. This is evidence that, as the surface becomes rougher, progressively higher plastic concentration is required for successful detection.

Table VI
SCATTERING VV ENR AND KS RESULTS BASED ON $S_{1,4}(f)$ RESPONSE MEASURED USING *SETUP1* FOR $H_s = 5,9,17$ CM, CONCENTRATIONS OF 10G/M^2, 20G/M^2, AND 40G/M^2 AND FREQUENCY BAND OF [2, 20] GHZ. BOLD VALUES INDICATE DETECTION FAIL.

H_s [cm]	Object [concentration]	Pol.	Freq. [GHz]	EnR	KS [%]
5	Spheres [10 g/m^2]	VV	2-20	1.51	9.9
	Spheres [20 g/m^2]			1.99	17.1
	Spheres [40 g/m^2]			2.41	23.4
9	Spheres [10 g/m^2]			1.45	9.6
17	Spheres [10 g/m^2]			**1.17**	**5.0**
	Spheres [20 g/m^2]			1.41	9.1
	Spheres [40 g/m^2]			1.92	17.8

F. Dependence on the frequency band

Given the previously identified scattering mechanisms, we expect an interplay between the frequency dependence of the random water surface scattering, and the target scattering. To find a potentially favorable band, we go back to the previous cases, and analyze the metrics separately for each predefined frequency sub-bands. For conciseness, we present results only for $H_s = 9\ cm$. Conclusions regarding frequency dependency are similar for $H_s = 5\ cm$ and $H_s = 17\ cm$, apart from the already mentioned observation that the overall detection degrades as H_s increases. Table X summarizes the metrics for PET bottles and PE tubes using *Setup1*.

Results indicate that, at least under the tested conditions, the floating plastic response increases with the frequency band, presents a maximum around 8-15 GHz (Xu to Kuu bands) and then decreases slowly beyond these bands. At the S-band, neither PET bottles and PE tubes are detected.

Table X
SCATTERING VV ENR AND KS RESULTS BASED ON $S_{1,4}(f)$ RESPONSE MEASURED USING *SETUP1* FOR $H_s = 9$ CM, CONCENTRATION 10 G/M^2 FOR DIFFERENT FREQUENCY BANDS. BOLD VALUES ARE USED TO INDICATE DETECTION FAIL.

H_s [cm]	Object [10g/m^2]	Pol.	Freq. [GHz]	EnR	KS [%]
9	PET bottles	VV	S	**1.07**	**2.3**
			Cu	**1.16**	**4.2**
			Ca	1.43	9.7
			Xu	1.61	9.8
			Xa	1.75	**11.9**
			Kuu	2.04	12.3
			Kua	1.65	9.1
			K	1.60	11.2
	5 cm PE tubes		S	**1.18**	**7.1**
			Cu	2.92	31.7
			Ca	7.45	47.5
			Xu	13	53.9
			Xa	9.74	50.8
			Kuu	10.4	41.6
			Kua	7.28	34.8
			K	4.63	30.1

V. DETECTION FRAMEWORK USING MACHINE LEARNING

Next, we analyze the feasibility of using a typical supervised ML workflow to detect floating macroplastics in the DELTARES scenario, based on the measured frequency response. Hence, before inputting any of our data onto the ML algorithm, we re-apply a FFT to each gated radar response used when computing the metrics.

In ML terms, detection is equivalent of performing a binary classification task, i.e., predict one of the two classes: plastic ('1') or no plastic ('0'). Thus, for each observation (response) we label data accordingly, using webcam images. However, since we also want to study the possibility of performing intraclass detection (distinguish between types of plastics), whenever we consider a multiclass scenario, we increase the label to account for the different types of plastics. For instance, considering PP spheres and PET bottle units, the former are labeled as class '1' whereas the latter is labeled as class '2'.

Our workflow is divided into the following steps: 1) Apply a Principal Component Analysis (PCA) to the dataset and perform feature reduction whilst accounting for 99% of the original variance in the dataset [33]; 2) Shuffle and split the dataset into training and validation subsets, 80 and 20% of the original size, respectively; 3) Use *k*-fold cross-validation (*k* = 5) on the training subset to obtain the best tuned and trained Support Vector Machine (SVM) model to perform the task at hand [34]; 4) Apply the SVM model to the validation subset; 5) Evaluate the robustness and generalization ability of the model to perform the task through the confusion matrix and accuracy (nº of correct predictions / total nº of predictions) [35]

We begin by evaluating the detection of 10 g/m^2 of PP spheres and PET bottles in 5 cm waves for both setups. In Figure 17 we can observe the confusion matrices output for *Setup1* (bottom) and *Setup2* (top). The accuracy for PP spheres and PET bottles is 74% and 82% for *Setup1* and 84% and 100% for *Setup2* , respectively. The scattering from the spheres is

more difficult to distinguish from the water background than the bottles. Still, with sufficient floating targets (skewed concentration as in *Setup2*), detection is possible. This observation is aligned with the EnR metric.

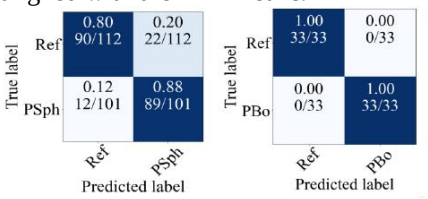

(a) *Setup*2 confusion matrix for PET Bottles (right) and PP Spheres (left)

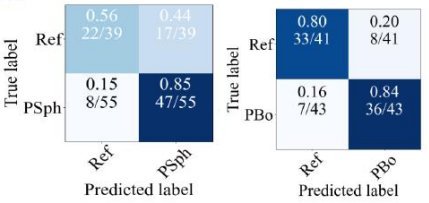

(b) *Setup*1 confusion matrix for PET Bottles (right) and PP Spheres (left)

Figure 17: S_2 radar scattergrams and supervised learning output of the MW datasets PBo_5^{10} and $PSph_5^{10}$.

Next, in Table XI, we summarize the detection of 10 g/m^2 of different floating targets for both setups in 9 and 17 cm waves. In both setups the accuracy accompanies the EnR, i.e., the detection in 9 cm waves is very good and deteriorates for 17 cm waves as the scattering from the reference units is more similar to the scattering from the target units. PE tubes have the most intense scattering and are detected in both 9 and 17 cm waves. For the PET bottles and straws in 17 cm waves, the EnR metric is closer to the threshold, but the accuracy is still 70% or above.

Table XI
COMPARISON OF ACCURACY (%) AND ENR METRICS FOR THE SEVERAL 9 AND 17CM MW DATASETS.

MW Datasets	S_1		S_2	
	Accuracy (%)	EnR	Accuracy (%)	EnR
$Bottles_9^{10}$	75	1.73	82	2.66
$Bottles_{17}^{10}$	50	1.70	76	1.48
$Straws_9^{10}$	82	2.41	87	2.12
$Straws_{17}^{10}$	70	1.36	72	1.14
$PE\ tubes_9^{10}$	93	9.93	94	3.26
$PE\ tubes_{17}^{10}$	86	5.29	82	1.64

Lastly, we consider the possibility of performing multiclass detection, e.g., intraclass of floating macroplastics, for the same 10 g/m^2 concentration. In Figure 18, we can observe the confusion matrices for 9 and 17 cm waves for setup *Setup1*. For these cases the accuracy is 64 and 43%, respectively. In line with the binary classification, in the multiclass case, for 9 cm waves, the SVM model was capable of defining the separation hyperplanes. However, since the intensity of the scattering from the different macroplastics is very similar, the misclassifications hamper the model detection. Lastly, for 17 cm waves, only the scattering response of the PE tubes is capable of defining an accurate hyperplane separating itself from the remaining classes.

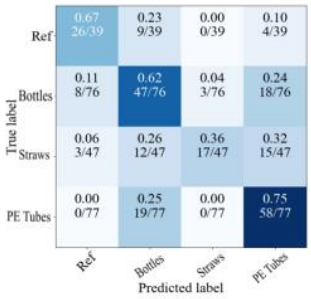

(a) 9 cm

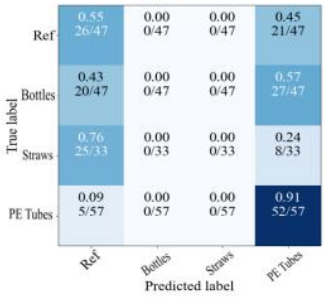

(b) 17 cm

Figure 18: Confusion matrices of the multiclass classification for 9 and 17 cm wave datasets of setup *Setup1*, top and bottom respectively.

VI. PLASTIC DETECTION IN OUTDOOR SCENARIOS

We extend the previous study to two outdoor scenarios, to assess the impact of uncontrolled environment conditions: namely its very short-term variation during the reference measurement and the measurement with targets; and the effect of capillary waves, which could not be tested indoor. One outdoor scenario is a pier (Figure 17) and the second scenario is the large estuary of the Tagus River in Lisbon (Figure 20). We label them *S*3 and *S*4, respectively.

A. The pier scenario

Scenario *S*3 is not significantly different from *S1* in terms of antenna heights and target distances, but capillary waves were present during the measurements. A single dual-polarization horn (DRH20E) antenna was used, with both ports connected to a VNA. Measurements, in backscatter mode, were carried out in the 2.5-20 GHz band. The antenna boresight was pointed at 45º incidence angle. The details are summarized in Table VII.

We measured different types of plastic targets under low and moderate wind, for all bands and sub-bands considered at DELTARES. However, for conciseness, we focus here only on 1.5-L plastic bottles case with wind blowing along direction $u2$ (Figure 17) with 17 km/h average velocity and 30 km/h gusts. Bottles were tied to a plastic net with 15 mm square mesh size, and 0.2 mm filament thickness (Figure 18). This prevented the bottles from spreading and therefore changing their concentration at the antenna's footprint during the measurement. It also prevented them from escaping into the ocean. Extensive experimental tests at DELTARES showed that this very thin 10 g/m^2 net is undetectable to the radar and has no measurable effect on the water spectrum.

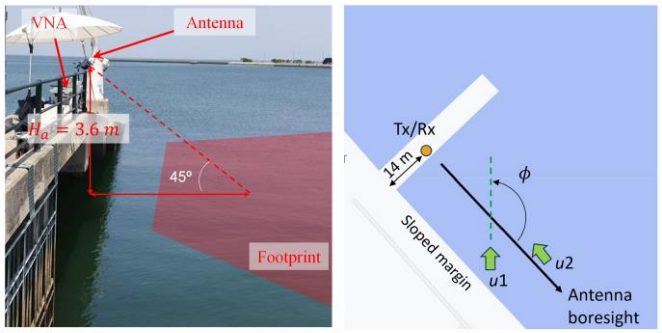

Figure 17: *S*3 outdoor pier scenario. (a) Measurement setup. (b) Top-view schematic with indication of wind direction.

Table VII
SUMMARY OF THE CONFIGURATION OF EACH SETUP USED OUTDOORS. "NA" REFERS TO "NOT APPLICABLE".

Setup	β	ψ	Freq. [GHz]	N_f	δt [s]	N_a
SScale	NA	45°	$2.5-20$	1601	0.8	1
Estuary	NA	45°	$9-10.5$	2401	1.2	2

Figure 19 shows, in the left panel, $I_{ij}^{cal,litter}$ for the reference measurements (i.e., without floating targets). Unlike previous indoor cases, the reference measurement presents high backscatter level, visible as the yellow band with variable stretch along distance, according to wind gusts. This enhancement of the backscatter is due to the capillary waves produced by the wind blowing along direction $u2$ (see Figure 17.b). The right panel of Figure 19) shows the scattergram for the same conditions but with the floating plastic bottles. The bottles' trails can still be identified, and the metrics indicate detection, with $EnR = 3.3$ and $KS = 14$. Similar results were obtained for HH polarization. This means that after using (3), the total scattered energy from the targets was higher than the contribution from the capillary waves.

Figure 18: Targets used in outdoor scenarios: (a) floating bottles attached a thin net in the pier scenario; (b) pink frame with seven 5L bottles, used in the estuary setup.

B. *Results for the large-scale Tagus River Estuary scenario*

Setup S4 is a much larger scale scenario, where the estuary is 2-km wide (Figure 18) and near the ocean. It has potential for observing capillary waves superimposed on short gravity waves; however, on the tests, only capillary waves were present. The antennas were installed at the "25 de Abril" bridge, which runs 75-m above the water. Two reflector antennas, with 33 dBi and 30 dBi were used for Tx and Rx respectively, connected to a V NA. The antenna footprint in this setup was around $12\,m \times 12m$. The look angle was 45°. (Table VII). The obtained license to use the spectrum for these experiments allowed only the 9 GHz to 10.5 GHz frequency range. Also, to compensate for the imposed limit on EIRP, an amplifier was used at the receiver port.

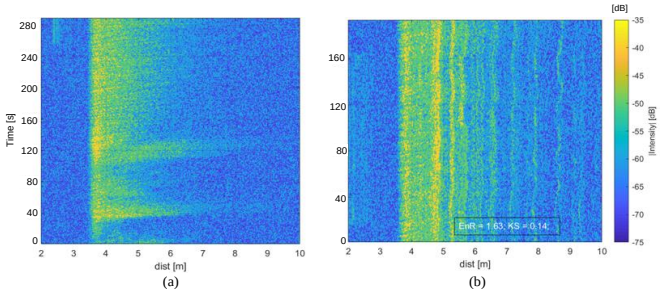

Figure 19: Scattering results, $I_{ij}^{cal,litter}$, based on VV backscattering measurement at Xa-band in *S*3 setup: (a) reference measurement; (b) net with bottles.

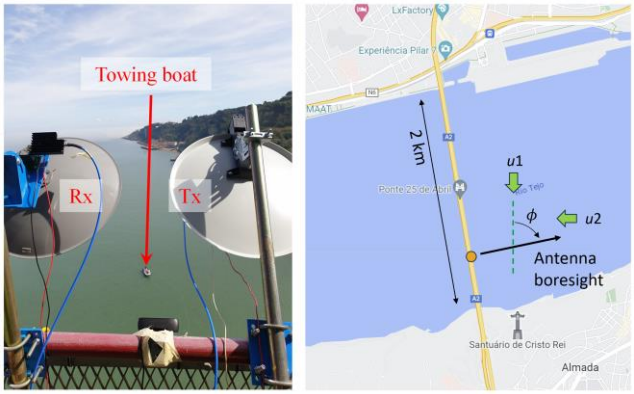

*S*4 scenario. Details of the measurement setup. (b) Top-view schematic of the scenario, with indication of wind direction.

The targets were formed by sets of 5-L plastic bottles attached to $1.2\,m \times 1.2\,m$ frames made of expanded polyurethane foam (see Figure 21). The target mass was roughly 1000 g, therefore, considering the antenna footprint area, the target had roughly a concentration of 10 g/m^2. This is the same concentration used in DELTARES experiments. Figure 21.b) shows the capillary wave pattern that was present during the measurements. To identify the antenna footprint limit, a trihedral corner reflector of 0.5-m side was scanned over the area of interest on the water. The corresponding backscatter was mapped onto the pixels of video acquired by a fixed camera on the bridge. This was essential to make sure the boat was far out of the antenna footprint.

The corresponding $I_{ij}^{cal,litter}$ scattergrams are shown in Figure 22.a) for the reference measurement, and in Figure 22.b) with the target inside the antenna footprint. The scattering intensity in the reference measurement changes gradually over time because of wind's intensity and direction fluctuation. The same happens with the background of Figure 22.b) for the same reason. In the latter figure, the target signature corresponds to the wiggling yellow trace. This shape resulted from the regular pulls from the boat to bring the target back into the antenna footprint, countering the river current. Although the target was

not always inside the antenna footprint, and the wind was not uniform, we calculated the metrics and obtained EnR =? and KS =?. We have positive detection, despite the capillary waves and despite the very low target concentration.

(a) (b)

Figure 21: Example of targets used in the *S*4 scenario. (a) Detail of the square frame made of Polyurethane foam and attached bottles. B) The target on the water, where a capillary wave pattern is visible.

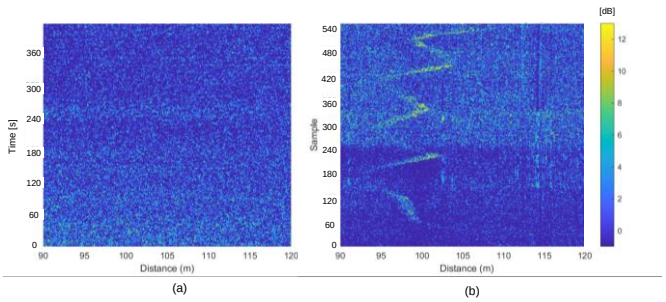

(a) (b)

Figure 22: Scattering results, $I_{ij}^{cal,litter}$, based on VV backscattering measurement at using estuary setup: (a) reference measurement; (b) pink frame with seven 5L bottles measurement.

VII. Radiometric Measurements

A limited-scale and larger-scale outdoor scenarios were considered for passive mm-wave measurements, using a WR-10 (75-110 GHz) radiometer: PMMW-10-0001. The first measurements were conducted in a garden-type 4.5 x 2.2 m^2 pool filled with 30 cm deep water. A tripod with the radiometer and a pan/tilt positioner was leaned against the shortest side of the pool, as represented in Figure 23.

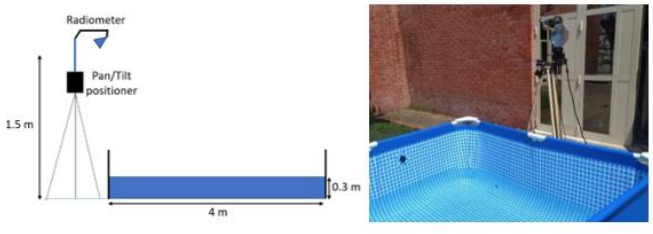

(a) (b)

Figure 23: Pool measurement setup: (a) schematic and (b) photograph..

The procedure consisted of sweeping a range of pan and tilt angles to obtain the object signature against the background. Some objects were tested with this setup, namely a PET bottle and Styrofoam tubes with different lengths (20, 10 and 5 cm). The objects were floating in the pool positioned at 50 cm horizontal distance of around from the radiometer. Two measurements were performed for each target: one with the object and another without. By subtraction the two, the response from the target could be obtained, as shown in Figure 24.

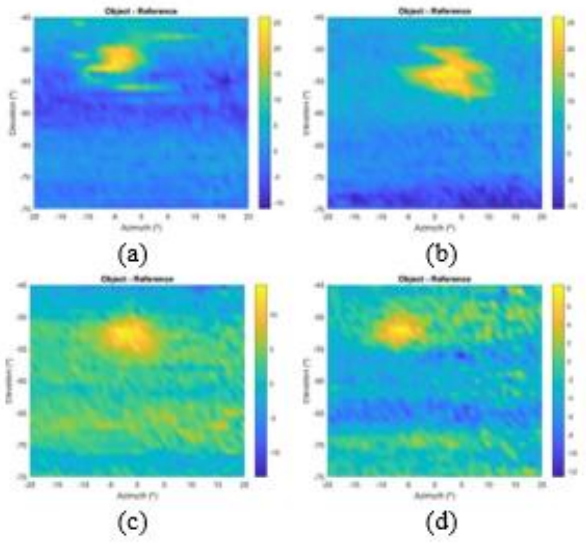

(a) (b) (c) (d)

Figure 24 - Pool radiometric measurements for object detection: (a) PET bottle; (b) 20cm foam tube; (c) 10cm foam tube; (d) 5cm foam tube.

All the objects were detected in the corresponding angles/distances, being the larger items the ones that led to both a higher difference to the reference and larger spot when subtracted from the reference, as expected.

The next step in the passive measurements was to test the radiometer in a more realistic and less controlled environment. Tests were performed in Jardim da Almoinha in Leiria. The radiometer was placed near the border of the water, marked with a red cross in Figure 25. The water presented some capillary waves, due to wind. Two test cases were measured: one with just water and the other with a PET bottle anchored to the bottom of the lake. The results are shown in Figure 25(b) where the bottle was again detected in the presence of capillary waves, meaning that the response of the bottle is higher than of the waves. The waves also led to movement of the bottle around the anchor point, contributing to a fuzzier image.

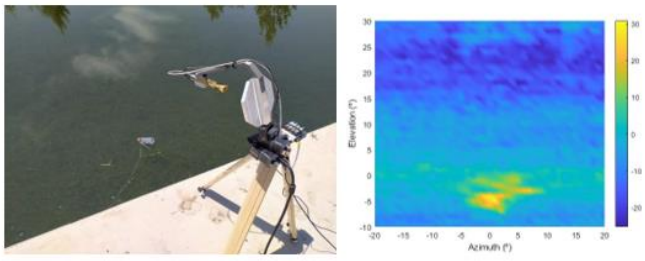

(a) (b)

Figure 25 - Lake radiometric measurements for PET bottle detection (a) photograph and (b) measurement subtraction.

All the tests performed using radiometric technology at the W-band showed that all objects cold be detected when floating on the water surface, as long as the measurements are performed outdoors, illuminated by the cosmic background radiation.

VIII. Conclusion

The study demonstrates that, under the tested conditions, the proposed formulation is effective to detect the presence of floating macroplastic using MW radar, down to 10 g/m^2. Our method is not based on image processing, but rather applies directly to the measured signal. The formulation benefits from the fact that the targets' speed is low, and the shape is constant, while the surface wave changes faster with time.

We started with measurements in indoor controlled environments, without considering other wind effects than those inherent to the JONSWAP low-wavenumber regime. This allowed focusing on fundamental aspects of the electromagnetic wave interaction with low-contrast floating targets, that would otherwise become hidden by the complexities associated with high wavenumber wind effects and its variability. The analysis in controlled environments showed that, at least for small plastic objects and low concentrations, one of the main contributors for the scattering are the deformations of the water contact surface caused by the object's weight. Thus, further to concentration, the detectability is influenced by the shape and size of the created indentations, angle of observation, wave significant height and frequency band. Most favorable frequency, under the tested conditions, was the X-Band and the lower part of the K-band.

We used a Machine Learning workflow to investigate if it can be used as an alternative strategy to deal with the problem of plastic detection. The results show that, after proper training, it can distinguish between the presence or absence of floating plastic, although it could not distinguish between different classes of floating plastic.

To assess our formulation in the high wavenumber regime, we extended the study to outdoor scenarios with the presence of wind. At least in one of the scenarios, the wind reached 17 km/h and 30 km/h gusts. Detection was possible in the tested cases. Bragg effects were not excessively strong, but the results are already indicative that the formulation can hold in some real scenarios. It will not be possible under all weather conditions, but there are conditions with wind where it can work. Detection probability will always be a function of the target size and concentration. For each sea state there will be certain target sizes and concentrations that, with our formulation, may stand out above the surface wave contribution.

The concept of energy ratio behind our formulation, based on the global response of the plastic litter patch, can be more effective for low cross-section sparse target distributions than other methods relying on the detection of individual targets as in image-based methods. This favors the application of our proposed method to a much larger distance from instrument to ground and wider patches of litter.

A more systematic assessment of our formulation for various wind forces and directions, including the case of composite surfaces with the two superimposed wave number scales, will be analyzed in a follow-up work.

Finally, we explored the feasibility of passive measurements for floating target detection. We observed that the detection was possible, not only in a very small-scale controlled scenario, but also in a medium scale pond. It was found, however, that it is an indirect detection, i. e. it is not the radiation emitted from the targets that we measure, but rather the shadow that targets cast on the cosmic background radiation that reaches the antenna through the reflection on the water surface.

References

[1] N. Maximenko, *et al.*, "Towards the integrated marine debris observing system," *Frontiers in Marine Science*, vol. 6, no. pp. 1-25, 2019.

[2] L. Lebreton, *et. al.* "Evidence that the Great Pacific Garbage Patch is rapidly accumulating plastic", Scientific Reports, vol. 8, Article number: 4666, 2018.

[3] (April 2022). United Nations (UN), "The 2030 Agenda for Sustainable Development". [Online]. Available: sdgs.un.org/goals.

[4] P. M. Salgado-Hernanz, *et al.*, "Assessment of marine litter through remote sensing: recent approaches and future goals," *Marine Pollution Bulletin*, vol. 168, p. 112347, Jul. 2021.

[5] K. Moy, *et al.*, "Mapping coastal marine debris using aerial imagery and spatial analysis," *Marine Pollution Bulletin*, vol. 132, pp. 52–59, Jul. 2018.

[6] S. P. Garaba and H. M. Dierssen, "An airborne remote sensing case study of synthetic hydrocarbon detection using short wave infrared absorption features identified from marine-harvested macro- and microplastics," *Remote Sensing of Environment*, vol. 205, pp. 224–235, Feb. 2018.

[7] K. Topouzelis, *et al.*, "Detection of floating plastics from satellite and unmanned aerial systems (Plastic Litter Project 2018)," *International Journal of Applied Earth Observation and Geoinformation*, vol. 79, pp. 175–183, Jul. 2019.

[8] K. Topouzelis, *et al.*, "Plastic Litter Project 2019: Exploring the Detection of Floating Plastic Litter Using Drones and Sentinel 2 Satellite Images," *IGARSS 2020 - 2020 IEEE International Geoscience and Remote Sensing Symposium*, pp. 6329–6332, 2020.

[9] L. Biermann, *et al.*, "Finding Plastic Patches in Coastal Waters using Optical Satellite Data," *Scientific Reports*, vol. 10, no. 1, p. 5364, Dec. 2020.

[10] O. Garcia-Garin, et al., "Who's better at spotting? A comparison between aerial photography and observer-based methods to monitor floating marine litter and marine mega-fauna," Environmental Pollution, vol. 258, p. 113680, Mar. 2020.

[11] J. A. Guffogg, *et al.*, "Towards the Spectral Mapping of Plastic Debris on Beaches," *Remote Sensing*, vol. 13, no. 9, p. 1850, May 2021.

[12] P. Tasseron, *et al.*, "Advancing Floating Macroplastic Detection from Space Using Experimental Hyperspectral Imagery," *Remote Sensing*, vol. 13, no. 12, p. 2335, Jun. 2021.

[13] K. Themistocleous, *et al.*, "Investigating Detection of Floating Plastic Litter from Space Using Sentinel-2 Imagery," *Remote Sensing*, vol. 12, no. 16, p. 2648, Aug. 2020.

[14] L. Goddijn-Murphy, and B. Williamson, "On Thermal Infrared Remote Sensing of Plastic Pollution in Natural Waters," *Remote Sensing*, vol. 11, no. 18, p. 2159, Sep. 2019.

[15] V. Martínez-Vicente *et al.*, "Measuring Marine Plastic Debris from Space: Initial Assessment of Observation

Requirements," *Remote Sensing*, vol. 11, no. 20, p. 2443, Oct. 2019.
[16] V. Raizer, Advances in Passive Microwave Remote Sensing of Oceans, *CRC Press*, 2017.
[17] N. Davaasuren *et al.*, "Detecting Microplastics Pollution in World Oceans Using Sar Remote Sensing*," IGARSS 2018 - 2018 IEEE International Geoscience and Remote Sensing Symposium*, Jul. 2018, pp. 938–941.
[18] G. Gennarelli, et al., "24 GHz FMCW MIMO Radar for Marine Target Localization: A Feasibility Study," *IEEE Access*, vol. 10, pp. 68240-68256, 2022.
[19] R. Somaraju and J. Trumpf, "Frequency, Temperature and Salinity Variation of the Permittivity of Seawater," *IEEE Transactions on Antennas and Propagation*, vol. 54, no. 11, pp. 3441-3448, Nov. 2006.
[20] R. O. Harger, and D. M. Levine, "Microwave scatter and sea state estimation: Two-scale ocean wave models," *Boundary-Layer Meteorol.*, vol. 13, pp. 107–118, 1978.
[21] L. Lebreton, *et. al.* "Evidence that the Great Pacific Garbage Patch is rapidly accumulating plastic", *Scientific Reports*, vol. 8, Article number: 4666, 2018.
[22] J. Krupka, "Measurements of the Complex Permittivity of Low Loss Polymers at Frequency Range From 5 GHz to 50 GHz," *IEEE Microwave and Wireless Components Letters*, vol. 26, no. 6, pp. 464-466, June 2016.
[23] T. Karpisz, *et al.*, "Measurement of Dielectrics From 20 to 50 GHz With a Fabry–Pérot Open Resonator," *IEEE Transactions on Microwave Theory and Techniques*, vol. 67, no. 5, pp. 1901-1908, May 2019.
[24] R. A. Martins, *et al.*, "Preliminary Characterization of Microwave Backscattering of Floating Plastic," *Telecoms Conference ConfTELE*, pp. 1 - 4, February, 2021.
[25] M. C. Evans and C. S. Ruf, "Toward the Detection and Imaging of Ocean Microplastics With a Spaceborne Radar," *IEEE Transactions on Geoscience and Remote Sensing*, vol. 60, pp. 1-9, 2022.
[26] M. Arii, M, *et al.*, "Applicability of SAR to Marine Debris Surveillance After the Great East Japan Earthquake," *IEEE Journal of Selected Topics in Applied Earth Observations and Remote Sensing*, vol. 7, no. 5, pp. 1729-1744, May 2014.
[27] (December 2022) DELTARES wave facility, Atlantic Basin, Delft, Netherlands. [Online] Available: https://www.deltares.nl/en.
[28] K. Hasselmann, *et al.*, "Measurements of wind-wave growth and swell decay during the Joint North Sea Wave Project (JONSWAP).," *Ergaenzungsheft zur Deutschen Hydrographischen Zeitschrift*, 1973.
[29] J. Frank, and Jr. Massey, "The Kolmogorov-Smirnov Test for Goodness of Fit", *Journal of the American Statistical Association*, vol. 46, no. 253, pp. 68-78, 1951.
[30] (April 2022). QRH20E - RF SPIN. [Online] Available: www.rfspin.com/product/qrh20e/.
[31] (April 2022) DRH30 – RF SPIN. [Online] Available: https://www.rfspin.com/product/drh30/
[32] J. M. Felício, " Study of a Universal Planar Antenna for Ultrawideband Applications," M.S. thesis, Instituto Superior Técnico, Universidade de Lisboa, Lisbon, Portugal, 2014. [Online]. Available: https://fenix.tecnico.ulisboa.pt/cursos/meec/dissertacao/2838286618788895]
[33] Jolliffe, Ian T. "Principal component analysis." Technometrics 45.3 (2003): 276.
[34] Cervantes, Jair, et al. "A comprehensive survey on support vector machine classification: Applications, challenges and trends." Neurocomputing 408 (2020): 189-215.
[35] Powers, David MW. "Evaluation: from precision, recall and F-measure to ROC, informedness, markedness and correlation." arXiv preprint arXiv:2010.16061 (2020).